Experimental thermal hydraulics study of the blockage ratio effect during the cooling of a vertical tube with an internal steam-droplets flow

Juan-David Peña-Carrillo, A. Oliveira, Alexandre Labergue, T Glantz, Michel Gradeck

Experimental thermal hydraulics study of the blockage ratio effect during the cooling of a vertical tube with an internal steam-droplets flow

J.D. Peña Carrillo[a,b], A.V.S. Oliveira[a,b], A. Labergue[a], T. Glantz[b], M. Gradeck[a,*]

[a] *LEMTA, UMR CNRS 7563, Université de Lorraine, Vandoeuvre-Lès-Nancy 54505, France*
[b] *IRSN, PSN/SEMIA/LIMAR, B.P. 3, 13115 Saint Paul-Lez-Durance, France*

Abstract

During a Loss of Coolant Accident (LOCA) in a Pressurized Water Reactor, partial or complete drying of fuel assemblies may take place. In these conditions, the fuel temperature increases and may lead to substantial deformation of the fuel rod cladding and a partial blockage of the fluid sub-channels. These regions could significantly affect the cooling capacity of the nuclear core during the reflooding phase by the emergency core cooling systems. Understanding the cooling process and the thermal-hydraulic characteristics of the flow in these deformed regions is decisive to guarantee nuclear safety. Looking to provide valuable experimental data to validate existing and new models, this work is an experimental study on the thermal hydraulics during the cooling of a vertical tube with an internal steam-droplets flow, representing the LOCA conditions at sub-channel scale. The effect of the blockage ratio on the tube temperature, heat dissipation, wall rewetting, and droplets characteristics is evaluated by testing three configurations (0%, 61% and 90%). Optical techniques were used for a comprehensive characterization of the process, being them infrared thermography, phase-Doppler analyzer and three-color laser induced fluorescence thermometry. In general, wall rewetting in the test section occurs from bottom to top, although there is a discontinuity in the rewetting front with the 90% blockage ratio configuration. The droplets diameter reduces downstream of the test section because of evaporation. Droplets breakup was specifically observed with 90% blockage ratio. In all the cases, the droplets temperature was approximately the same up- and downstream of the test section, which indicates they are in nearly thermal equilibrium state and, therefore, representative of a LOCA situation.

Keywords:
LOCA, Thermal hydraulics, Steam-droplets flow, Infrared thermography, Phase Doppler measurements, Laser Induced Fluorescence thermometry

Nomenclature

Greek Letters

β	thermal sensitivity of the fluorescence signal	Φ	rate of heat flow
		ρ	density
		τ_b	blockage ratio
μ	dynamic viscosity	φ	heat flux

*Corresponding author
Email address: michel.gradeck@univ-lorraine.fr (M. Gradeck)

Roman Letters

$\dot{m}$	mass flow rate
a,b,c	3cLIF calibration coefficients
Bi	Biot number
C	fluorescent dye concentration
C_p	specific heat
D	diameter (tube)
d	diameter (droplets)
I	laser intensity
I_f	fluorescence intensity
K	equation parameter
K_M	Mundo number
L	length
N	amount of data
P	perimeter
r	radius
R_f	fluorescence intensity ratio
Re	Reynolds number
S	cross-sectional area
St	Stokes number
T	temperature
t	time
u	axial velocity
V_c	3cLIF collection volume
We	Weber number
z	axial position

Subscripts

∞	ambient
0	reference condition for 3cLIF measurements
b	deformed region
c	convection
crit	critical
d	droplets
ext	external
h	hydraulic
i	spectral band of detection
int	internal
j	droplets diameter class
k	conduction
l	injection liquid
loss	heat losses
nb	not-deformed region
opt	optical layout
r	radiation
s	steam
spec	fluorescent dye properties
t	tube
up	upstream
w	wall

1. Introduction

Loss Of Coolant Accident (LOCA) is a hypothetical accident that can occur in a Pressurized Water Reactor (PWR) where there is a break in the primary circuit of a nuclear power plant, which causes a sudden pressure drop and evaporation of the flowing water. By consequence, the heat generated by the nuclear fuel rod in the core can no longer be dissipated, increasing their temperature and causing the ballooning of fuel rods claddings that can even burst. To avoid the fuel temperature to reach critical values (like the limit of 1477 K for the cladding temperature [1]), emergency core cooling systems (ECCS) work to reflood the reactor's core and cool down the fuel assemblies.

An illustrative graphic of this process is shown in Figure 1. Although the probability of a LOCA taking place is very low, the severity of such accident is immense, making this event a key factor to guarantee nuclear safety.

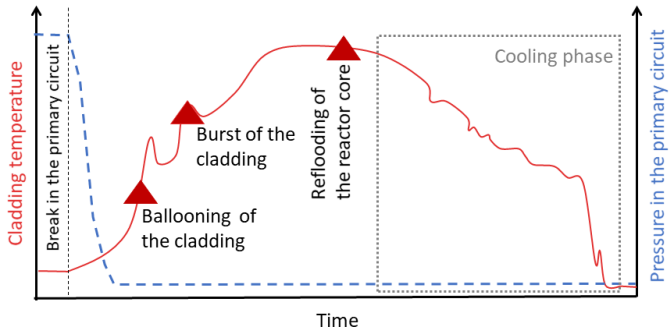

Figure 1: Temporal evolution of the cladding temperature (solid line) and water pressure (dashed line) during a LOCA.

The mentioned events of claddings deformation and burst are problematic during the reflooding phase once they locally decrease the cross-section area of the flow passage. This phenomenon was shown by the Institut de Radioprotection et de Sûreté Nucléaire (IRSN) during the PHEBUS-LOCA experimental program in the 1980s, where they simulated LOCA conditions and observed the final state of the fuel assembly [2]. Figure 2 shows a picture of one test, being evident the deformation and bursting of some fuel claddings, as well as the formation of deformed sub-channels.

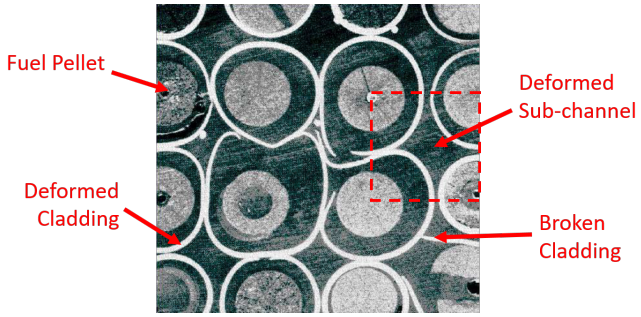

Figure 2: Fuel claddings after a LOCA simulation during a PHEBUS-LOCA experiment [2].

The cooling of fuel rods during the reflooding phase, which is highlighted in Figure 1, is a very complex process mainly because of the occurrence of different heat and mass transfer phenomena, but also because of the complex geometry resulted by the cladding ballooning, as presented in Figure 3. With the rise of the reflooding level, the quenching front advances as well and generates droplets (due to spattering and bursting effects) and steam at the triple interface of solid-liquid-vapor. At this location, we find liquid water at nearly saturation temperature and wall temperatures above the Leidenfrost point. Moreover, droplets are also generated at the liquid-vapor interface due to the shearing effect. Therefore, the cladding cooling upstream of the quenching front is performed at first by a two-phase mist flow of superheated steam and droplets at saturated temperature, and further by a single-phase flow of superheated steam, as all droplets completely evaporate. Previous works have presented some characteristics of the two-phase flow found in LOCA conditions [3–5]:

- Droplets: near to saturation temperature, diameters between 50 μm and 1000 μm and volumetric fraction

between 10^{-4} and 10^{-2};

- Steam: temperature up to 800 °C and pressure up to 3 bar;
- Fuel cladding: temperature between 300 °C and 1200 °C and emissivity between 0.5 and 0.8.

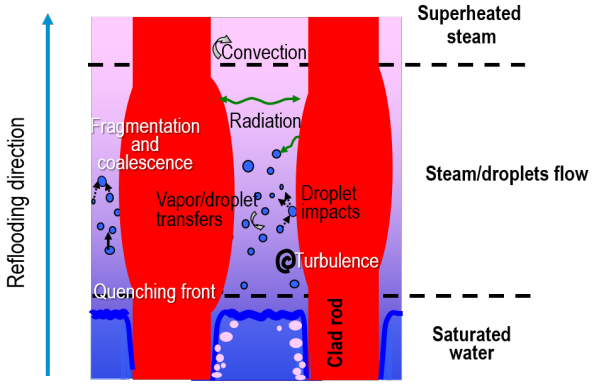

Figure 3: Heat and mass transfer phenomena during LOCA with ballooning of fuel claddings.

Even though much effort has been done in the past to evaluate the cooling phase during a LOCA, as Grandjean presents in his review of experimental campaigns performed in the 1980's [6], these subjects are still being investigated today in both experimental [3, 7–9] and modeling works [4, 10, 11]. Understanding in detail the physics during the cooling phase is crucial for safety requirements to guarantee the long-term coolability of the nuclear core and its structural resistance.

With this perspective, IRSN launched the project PERFROI ("**PER**te de re**FROI**dissement" in French, which means "loss of cooling") to deeply investigate the thermomechanical and thermal hydraulics processes in LOCA conditions [2]. While studies on the thermo-mechanical axis are aimed at the evaluation of claddings deformation, oxidation, and failure during heating and quenching, the ones on the thermal hydraulics axis look forward to answer questions like what is the maximum blockage ratio during LOCA that is still coolable by the mist flow or what is the effect of fuel relocation on the peak cladding temperature. We can only answer these questions with detailed data of the two-phase flow and quantitative analyses of the heat transfer paths. This information would allow numerical simulations to accurately estimate the cladding temperature in different conditions of LOCA by varying parameters like blockage geometry and steam mass flow.

Hence, the present work is an experimental investigation at a sub-channel scale of the cooling phase in LOCA conditions, evaluating the effect of the blockage ratio on the temperature, internal heat dissipation, rewetting of the wall and droplets characteristics like diameter, velocity and temperature. We performed all the measurements on the test section with optical techniques, eliminating the effects of the presence of sensors, which has always been used in previous works (like thermocouples). These experiments provide valuable data to validate mechanistic models for further use in numerical tools, as IRSN's DRACCAR code [12].

2. Experiment at sub-channel scale

Although performing tests at sub-channel scale neither represents a real geometry of a nuclear reactor nor includes the by-pass effect (the preferred steam flow through regions without deformation), this experimental approach allows having a highly-controlled environment to evaluate in detail parametric and geometric effects. Furthermore, at sub-channel scale experiments, we can use optical techniques for a global characterization of the surface temperature and the internal mist flow. For example, the use of an infrared camera to evaluate the surface temperature is not feasible in a nuclear-like geometry, which demands the use of thermocouples.

In nuclear reactors, a sub-channel is defined as the volume of fluid between four neighboring fuel rods (Figure 4), which can be formed by not-deformed or deformed claddings, giving the respective cross-sectional areas of S_{nb} and S_b.

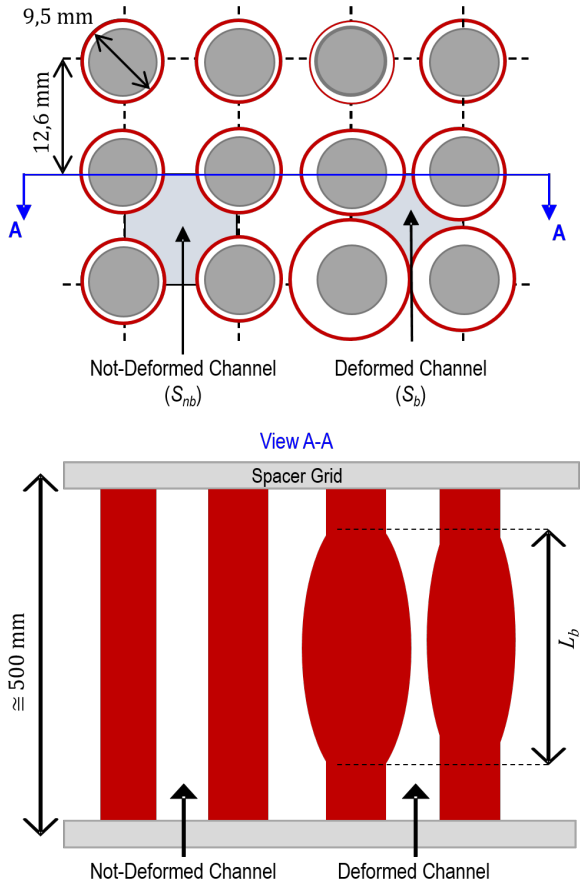

Figure 4: Illustrative drawing of a sub-channel representation.

Two parameters are commonly used to characterize a deformed sub-channel. The first is the *blockage ratio* τ_b, expressed by:

$$\tau_b = 1 - \frac{S_b}{S_{nb}} \tag{1}$$

which gives the reduction in the sub-channel cross-sectional area because of the cladding deformation. Hence, a 0% blockage ratio would be a non-deformed sub-channel, and a 100% blockage ratio would be a completely blocked

sub-channel. Two typical values of blockage ratio are 61%, where the four neighboring claddings are deformed, in contact, and keeping a circular profile; and 90%, one of the highest blockage ratios found in previous experiments [13]. The second parameter is the *blockage length* L_b (Figure 4), which is limited by the distance between two spacer grids (about 500 mm), although common values in previous tests are never higher than 250 mm [6].

For a better analysis of the test results to evaluate the blockage ratio effect and to simplify later validations of mechanistic models, we used circular tubes to represent the sub-channel in the present work. The choice of the tube diameter ensures the same hydraulic diameter D_h of the sub-channel, which was calculated with:

$$D_h = \frac{4S}{P} \tag{2}$$

where S and P are the wetted surface area and the wetted perimeter, respectively. For instance, the calculated hydraulic diameter for the case with no deformation is 11.78 mm. Taking this diameter as the reference for $\tau_b = 0$, we can calculate the proper diameter of a contraction with Equation 2 to have a desired blockage ratio by using the deformed cross-sectional area S_b calculated with Equation 1. Hence, a diameter of 7,35 mm gives a blockage ratio of 61%, while 3,72 mm results in a 90% blockage ratio.

3. Experimental set-up and methodology

Figure 5 presents an illustrative drawing of the experimental set-up named **CO**o**LI**ng of **B**lockage **R**egion **I**nside a PWR Reactor (COLIBRI), which consists of a test section, a supply system of droplets generator and another of superheated steam.

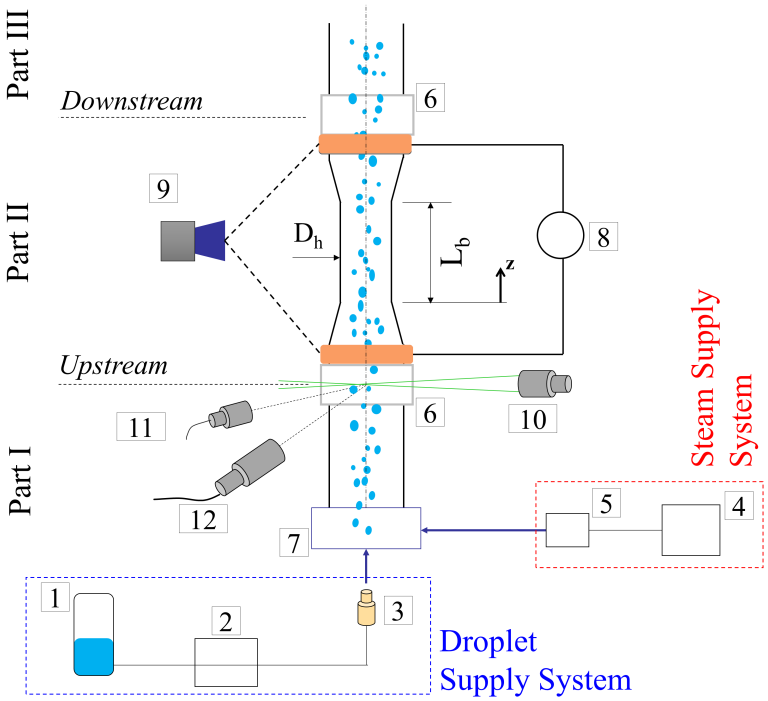

Figure 5: Schematic diagram of COLIBRI experimental set-up. 1) Pressurized water tank; 2) Water preheater; 3) Droplet generator; 4) Electric boiler; 5) Steam superheater; 6) Optical measurement windows; 7) Steam/droplets mixer; 8) DC power source; 9) Infrared camera; 10) Laser probe; 11) LIF detector; and 12) PDA detector.

The test section is made of Inconel-625 and is divided into three parts. Parts I and III are fixed tubes with 0.57 mm thickness and 11.78 mm internal diameter, which corresponds, respectively, to a typical rod clad thickness and to the hydraulic diameter of a non-deformed PWR sub-channel. Also, Part I is 300 mm long to ensure a developed flow at its outlet ($L/D_h = 25$). Part II is a removable Venturi tube and is heated by Joule effect with the use of a DC power source (TDK Lambda Genesys 2U series GEN 10V-330A, 3,3 kW max).

This removable piece allows testing different geometrical configurations to represent a partially deformed sub-channel by using an equivalent hydraulic diameter. Table 1 presents the tested configurations with different blockage ratios and lengths, while Figure 6 presents detailed drawings of Part II for the configurations of 61% and 90% blockage ratios. Note that the converging and diverging angles for both configurations are kept the same, so, for this reason, they have different lengths. The tube used in the 0% configuration is 175 mm long. Moreover, the wall thickness is specifically chosen for each case to ensure similar thermal inertia between the test-section configurations, parameters that could affect the test results [6]. Furthermore, the use of different wall thicknesses provides a constant cross-sectional area of the tube along its length, including the converging and diverging parts in the 61% and 90% configurations. By consequence, the linear electrical resistance is kept approximately the same and this results in a homogeneous heating of the tube and a more uniform temperature profile. This way, we were able to reduce side-effects and better analyze the blockage ratio effect on the cooling of the tube.

Table 1: Configurations of the test section (Part II)

Configuration	**1**	**2**	**3**
Blockage Ratio (τ_b)	0%	61%	90%
Equivalent Hydraulic Diameter (D_h)	11.78 mm	7.35 mm	3.72 mm
Blockage Length (L_b)	-	100 mm	100 mm
Wall Thickness	0.57 mm	0.95 mm	1.45 mm

We placed optical accesses made of borosilicate glass up- and downstream of Part II to measure the droplets characteristics with optical techniques. We measured the droplets diameter and velocity using a Phase Doppler Analyser (PDA) and their mean temperature with a Laser Induced Fluorescence (LIF) technique. These methods are described in sections 4.2 and 4.3.

A dispersed two-phase flow of steam and droplets is supplied upstream of Part I of the test section. A steam generator (AURA MA 6 kW) and a superheater (AURA S2000 2 kW) provides the steam at temperatures up to 200 °C. The steam line is insulated to decrease heat losses to the ambient. An orifice flowmeter measures the mass flow rate of the steam, while a pressure transducer and a K-type thermocouple measure the steam pressure and temperature, respectively.

Meanwhile, a piezoelectric injector (FMP Technology) produces the droplets of the dispersed flow with diameters up to 500 μm and a maximum flow rate of 2 kg/h, hence we can comply with the two-phase flow characteristics found in LOCA conditions. However, we can adjust both the droplets size and the flow rate by changing the injectors orifice or the injection pressure. An isothermal bath preheats the fluid before the injection up to 80 °C.

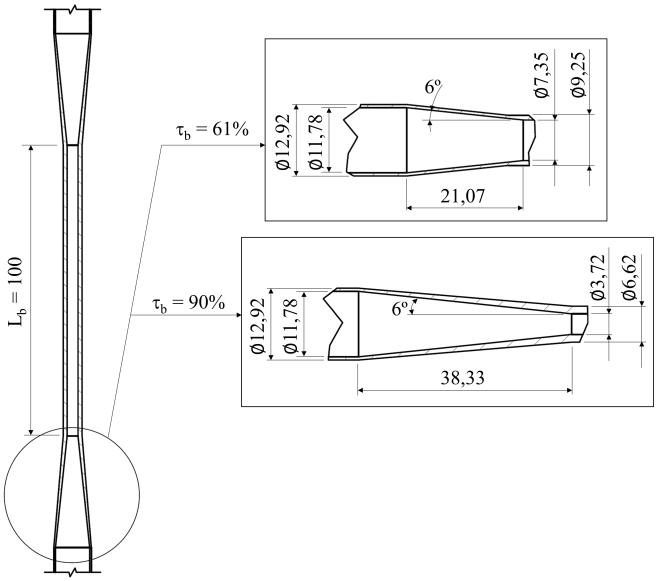

Figure 6: Detailed drawing of Part II for the configurations of 61% and 90% blockage ratios.

It is worth mentioning that, in the present experiment, we used deionized water in both the steam and the liquid lines.

To evaluate the cooling phase of the test section, we performed the experiments with the following procedure (Figure 7 presents each step in a graphic for a better understanding of the test):

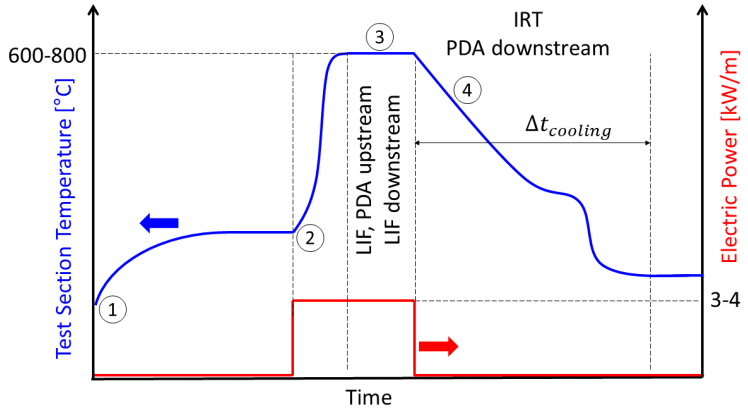

Figure 7: Graphical illustration of the test procedure. (1) Start of the steam flow; (2) Start of the droplets injection and heating of the test section; (3) Measurement of the droplets characteristics; and (4) Cooling experiment.

1. *Start of the steam flow:* At the beginning, the experimental apparatus is at ambient temperature. The steam flow is started to take the adjacent components close to the steady-state condition, including the test section. This procedure, which takes place for about one hour, avoids the possibility of the steam condensation on surfaces, including the optical accesses.
2. *Start of the droplets injection and test section heating:* Once steady state is achieved, we started both the droplets injection and the heating of Part II of the test section. The test section temperature increases up to a new steady-state value between 600 °C and 800 °C, which is a representative temperature of a LOCA.

3. *Measurement of the Droplets Characteristics:* As the LIF technique cannot acquire data with the same rate of the PDA system, the droplets temperature are measured at this step (before the cooling experiment), up- and downstream of the test section. We also measure the droplets diameter and velocity with PDA at this moment, once a large number of droplets are collected to better determine the initial condition of the dispersed flow.
4. *Cooling Experiment:* After the two previous steps, the cooling test begins. The power source of the test section heating is switched off and the IRT and the PDA downstream simultaneously record the transient of the test section temperature profile and the droplets diameter and velocity, respectively.

Table 2 provides the ranges of the experimental conditions explored in this work. The experimental conditions respect typical values found in LOCA. However, the steam temperature is in the lower range of actual LOCA conditions. Jin et al [14] present in their experimental study with a 7x7 fuel rod bundle that the steam temperature is near saturation in the near field, which is the region close to the quenching front. Contrarily, far downstream of the quenching front, the steam temperature can be superheated by several hundred, reaching practically the same temperature as the fuel rod. Although in this work we did not perform the experiments at very high steam temperatures, the present conditions are appropriate to provide detailed data for the validation of mechanistic models and simulation codes.

Table 2: Range of the experimental conditions

Parameter	**Range**
System Pressure	1.0 bar – 1.3 bar
Injection Mass Flow Rate	0.8 kg/h
Droplets Temperature (Injection)	62 °C – 63 °C
Droplets Diameter (Injection)	5 μm – 300 μm
Steam Mass Flow Rate	3.7 kg/h – 4.8 kg/h
Steam Temperature	166 °C – 170 °C
Volumetric Fraction of Droplets	1.10^{-4} – 2.10^{-4}
Initial Wall Temperature	600 °C – 700 °C

4. Measurement techniques and uncertainties

4.1. Infrared Thermometry (IRT)

4.1.1. Measuring the temperature profile

The outer surface temperature of the test section was measured with the use of an infrared (IR) camera (Cedip Jade III, number 9 in Figure 5) at a frequency of 50 Hz, using the spatial resolution of 320x240 pixels and a narrow wavelength filter ([3.97-4.01] μm). We applied a thin layer of high-temperature paint on the test section surface to increase its emissivity (found as 0.84 using an Ulbricht sphere) and, consequently, increase the quality of the measurements.

To better explain the IRT application in this work, we should first present the assumptions made in the test section. Figure 8 presents the energy balance on a differential element of the tube, where φ_{int} is the heat flux dissipated

by the internal two-phase flow, φ_r and φ_c are the respective heat fluxes dissipated to the ambient by radiation and free convection through the outer surface, and φ_k the conductive heat flux due to temperature gradients within the thickness of the tube.

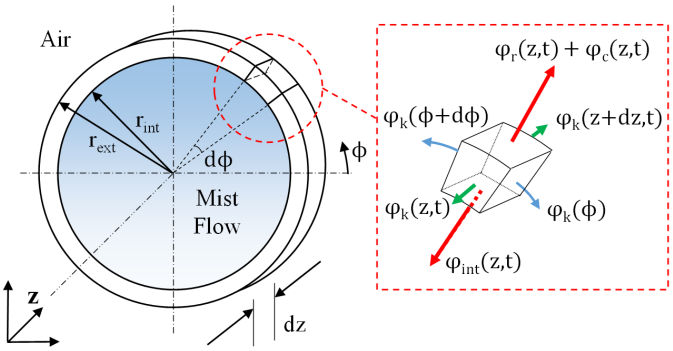

Figure 8: Schematic illustration of the heat transfer paths on a differential element of Part II in the test section.

The first hypothesis establishes that the tube temperature gradient in the radial direction r is negligible because $Bi \ll 1$ for all the test cases. Hence, $T_w(r, z, \phi, t) = T_w(z, \phi, t)$, being T_w the tube temperature.

The second hypothesis is considering uniform temperature in the tube's azimuthal direction (ϕ in Figure 8), hence $\varphi_k(\phi) = \varphi_k(\phi + d\phi) = 0$, so T_w varies only in the axial position z and time t, resulting in $T_w(z, \phi, t) = T_w(z, t)$. This means that the tube temperature profile is axisymmetric and can be measured at any position ϕ. However, we could have misleading results near the curvature of the tube, as the measurement of the radiative intensity is dependent on the angle of view between the measuring surface and the IR camera. Therefore, we only used pixels near the tube centerline for the temperature measurements, as presented in Figure 9a. Then, being established the region of analysis, the digital levels of pixels at the same axial position were averaged to obtain the tube temperature for each point z.

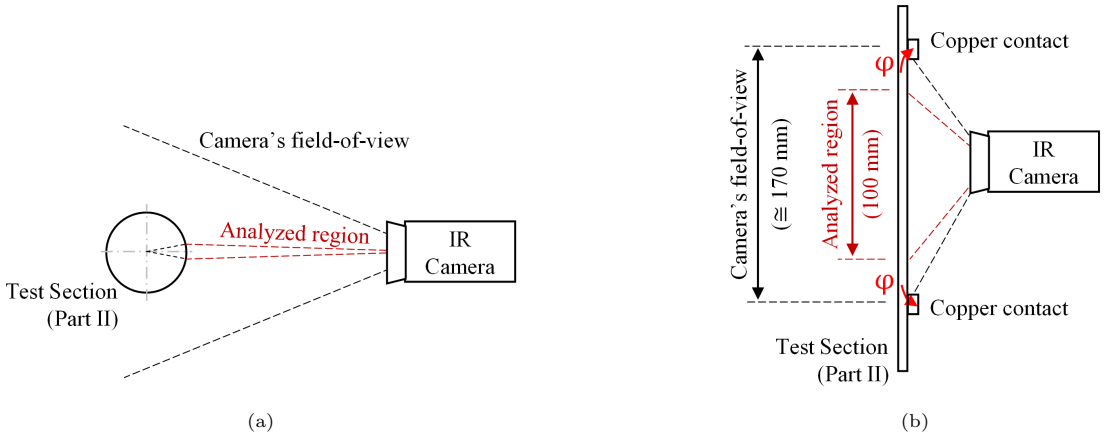

Figure 9: Analyzed region on Part II of the test section.

The third hypothesis regards the heat losses of the test section by thermal conduction through the copper contacts. In our experimental apparatus, the distance between the electrical contacts is approximately 170 mm. During data processing of the IRT, we observed that the temperature gradients are nearly zero at pixels 30 mm away from the

extremities. As the length of the analyzed region is 100 mm (presented in Figure 9b), which is the length of the blockage ratio in study, the pixels affected by the borders are not considered during the study and, consequently, the thermal losses by conduction through the contacts become negligible.

An *in-situ* calibration method was established to correlate the surface temperature and the camera digital level (its output signal proportional to the radiative intensity), which consisted of a simultaneous and synchronized measurement of the test section temperature with the IR camera and a K-type thermocouple during a natural convection cooling process (no internal flow). Then, we could find a fitting curve to model the temperature as a function of the IR digital level. In all the tests of the present work, the deviation between the model and the measured by the thermocouple was always below 5 °C, which we can consider as the temperature uncertainty in the IRT. This calibration procedure took place before every single test to guarantee the best accuracy of the IRT.

4.1.2. Estimating the internal heat flux

The heat flux dissipated by the internal two-phase flow (φ_{int}) was estimated by using the energy balance on the test section already shown in Figure 8. The mathematical expression for this balance is:

$$\varphi_{int}(z,t) = -\left(\frac{S_t \rho_w C_{p,w}}{\pi D_{int}}\right)\frac{dT_w(z,t)}{dt} - \left(\frac{D_{ext}}{D_{int}}\right)\varphi_{loss}(z,t) \tag{3}$$

where S_t, ρ_w, $C_{p,w}$, D_{int}, and D_{ext} are, respectively, the cross-sectional area, the density, the specific heat capacity, the internal diameter, and the external diameter of the test section. The summation of all the heat losses of the element (radiative, convective and conductive) is given by φ_{loss}, hence:

$$\varphi_{loss}(z,t) = \varphi_r(z,t) + \varphi_c(z,t) + \varphi_k(z,t) \tag{4}$$

The radiative heat flux φ_r is calculated using the Stefan-Boltzmann equation, while the free-convective heat flux φ_c is estimated with the Nusselt number using a vertical plate correlation and the conductive heat flux φ_k is calculated with Fourier's Law [15]. Preliminary simulations showed that the contribution of φ_k could be neglected compared to φ_r and φ_c. We validated the estimation of the heat losses by performing an experiment without any internal flow in the test section. The result is shown in Figure 10, where we find a great match between experimental data and calculated heat losses with Equation 4 considering $\varphi_k(z,t) = 0$.

The uncertainty of φ_{int} is estimated to be approximately 10% after propagating the error of each parameter in Equation 3.

4.2. Phase Doppler Analyser (PDA)

We measured the droplets diameter and velocity up- and downstream of Part II of the test section with the use of a PDA manufactured by Dantec-Dynamics®. PDA technique is an extension of LDA (Laser Doppler Anemometry) but using at least two photo-detectors. A comprehensive survey on PDA measurements may be found in Albrecht et al [16] This includes a classic-PDA reception optics and a P80 signal processor. The laser excitation volume is generated by an LDA transmitter probe (Dantec-Dynamics Fiber Flow probe®) and with the green line ($\lambda = 514.5$ nm) of an argon-ion laser. The PDA apparatus operates in the first refraction mode with a 60° off-axis angle. Here, only the axial velocity component (u_d), i.e., along the z axis, is measured. The front lenses of the transmitter probe

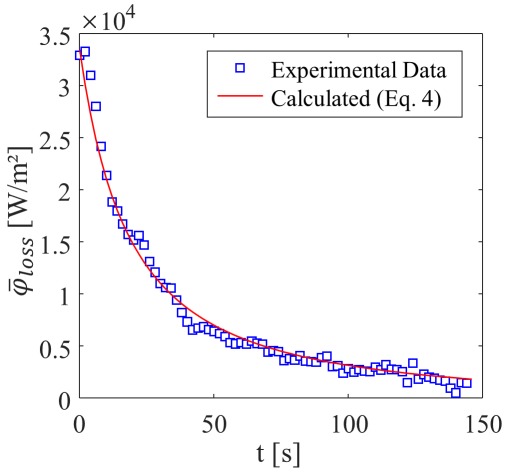

Figure 10: Validation of the estimated heat loss through the outer surface of the test section with no internal flow.

and the receiver have focal lengths of 1200 mm and 310 mm, respectively, giving a maximum measurable droplet diameter of 300 μm. A spherical validation of 25% is chosen, rejecting less than 10% of all detected droplets. The uncertainties of PDA measurements are not evident to evaluate since they depend on strongly correlated parameters, as the optical configuration (mainly the angle position and focal lengths of both receiver and transmitter probes), the photomultiplier high-voltage, and the electro-optical gain. According to previous studies [17, 18], by using repetitive measurements, global errors for both velocity and diameter are evaluated of 5% and 10% respectively.

4.3. Three-color Laser Induced Fluorescence (3cLIF) Thermometry

Droplet temperature are measured by Laser Induced Fluorescence (LIF) thermometry. The technique is based on the thermal dependency of a fluorescent dye dissolved in water at a low molecular concentration. Fluorescence spectrum is broadband and the fluorescence intensity $I_{f,i}$ at a given wavelength may be expressed by [19]:

$$I_{f,i}(T) = K_{opt,i} K_{spec,i} V_c I C e^{\frac{\beta_i}{T}} \tag{5}$$

where K_{opt} and K_{spec} are parameters depending on the optical layout and the fluorescent dye properties respectively, V_c is the collection volume of the fluorescence photons, I is the laser excitation intensity, C is the fluorescent dye concentration, β_i is the temperature sensitivity of the fluorescence signal at the wavelength i, and T the absolute temperature of the water-dye solution. Generally, V_c, I and C are unknown and may be removed by measuring the fluorescence intensity ($I_{f,1}$ and $I_{f,2}$) on two spectral bands having different temperature sensitivities (say 1 and 2), and by calculating their ratio (R_{f12}). Eventually, a single reference R_{f120} at a known temperature T_0 is performed to eliminate both K_{opt} and K_{spec}. Thus, a normalized fluorescence ratio is obtained:

$$\frac{R_{f12}(T)}{R_{f120}(T_0)} = e^{\beta_{12}\left(\frac{1}{T}-\frac{1}{T_0}\right)} \tag{6}$$

with $\beta_{12} = \beta_1 - \beta_2$. This method is referred as 2cLIF for two-color LIF. Nevertheless, according to previous studies [20, 21] when a polydispersion of the droplet diameter occurs, it is necessary taking into account the droplet diameter. A third spectral band of detection, strongly dependent on the droplet diameter, is introduced and a second normalized

fluorescence ratio R_{f32} is obtained. Finally, an equation correlating fluorescence ratios only with the temperature may be derived [21]:

$$\frac{R_{f12}}{R_{f120}} e^{\beta_{12}\left(\frac{1}{T_0}-\frac{1}{T}\right)} = a\left[e^{\beta_{32}\left(\frac{1}{T_0}-\frac{1}{T}\right)}\frac{R_{f32}}{R_{f320}}\right]^2 + b\left[e^{\beta_{32}\left(\frac{1}{T_0}-\frac{1}{T}\right)}\frac{R_{f32}}{R_{f320}}\right] + c \tag{7}$$

with R_{f320} the reference of the second fluorescence ratio at the temperature T_0 and $\beta_{32} = \beta_3 - \beta_2$. We obtain the parameters a, b and c during a calibration phase as described in Labergue et al [21]. This technique is now referred as 3cLIF because of the use of three spectral bands. Both constants β_{12} and β_{32} are determined from a temperature calibration phase according to a similar process presented in Depredurand et al [22].

In the present work, we used sulforhodamine-B on deionized water at a concentration of 5.10^{-6} mol/l. The selected spectral bands are:

- First spectral band: [535-545] nm,
- Second spectral band: [615-700] nm, and
- Third spectral band: [555-570] nm.

The uncertainty of the 3cLIF thermometry is dependent not only on the ratios of fluorescences (which have their own uncertainties) but also on the calibration of the parameters. Furthermore, the number of collected droplets by the 3cLIF apparatus is not as large as with the PDA, being around a few hundred collected in several minutes, because of the low signal-to-noise ratio intrinsic to the method. Consequently, similarly to the PDA, the calculation of the droplet temperature uncertainty is not evident. Following the analysis of Labergue et al. [21], we also found in the present study a statistical error of the fluorescence ratios of 1%, which leads to a 5 °C uncertainty for the droplets temperature.

4.4. Other parameters

Finally, the steam and liquid temperatures have an accuracy of 1 °C, the measured pressures of 1.5%, the steam mass rate of 0.90%, and the liquid mass rate of 2%.

4.5. Summary of the techniques

Table 3 presents a summary of the presented techniques and their post-processed outputs that allows us to analyze the cooling phase process and the blockage ratio effect.

Table 3: Summary of the post-processed parameters from the three main techniques used in the present work.

Technique	**Parameters**	
Infrared Thermography (IRT)	Surface temperature T_w Unit: °C Variables: z, t	Internal heat flux φ_{int} (estimated with Eq. 3) Unit: W/m^2 Variables: z, t
Phase Doppler Analyser (PDA)	Droplets diameter classes d_d (up- and downstream of Part II) Unit: μm Variable: t	Droplets velocity classes u_d (up- and downstream of Part II) Unit: m/s Variable: t
Three-color Laser Induced Fluorescence (3cLIF) Thermometry	Droplets mean temperature $\widetilde{T}_d$ (up- and downstream of Part II, before the cooling phase) Unit: °C Variable: -	

5. Results and discussion

For a better presentation and analysis of the test results, we used two different types of mean values: spatial and arithmetic. Especially used for the tube temperature T_w, the spatial mean value $\overline{T}_w$ of the temperature profile in z is defined by:

$$\overline{T}_w = \frac{\sum_{k=1}^{N_w} T_{w,k}(z)}{N_w} \tag{8}$$

where N_w is the number of pixels from the IRT in the length of the test section at an instant t during the cooling phase. Meanwhile, the classic arithmetic mean value $\widetilde{x}$ of a parameter x is calculated by:

$$\widetilde{x} = \frac{\sum_{k=1}^{N} x_k}{N} \tag{9}$$

where N is the amount of data of the population in the analysis.

Table 4 shows the inlet test conditions during the cooling phase for each configuration, being $\widetilde{\dot{m}}_s$ the average steam mass flow, $\widetilde{T}_s$ the average steam temperature, $\widetilde{\dot{m}}_l$ the average liquid injection mass flow, and $\widetilde{T}_l$ the average liquid temperature before injection. We can see they are similar for all the test cases, which makes possible the evaluation of the blockage ratio effect.

Table 4: Inlet test conditions for each experience

Config.	τ_b **(%)**	$\widetilde{\dot{m}}_s$ **(kg/h)**	$\widetilde{T}_s$ **(°C)**	$\widetilde{\dot{m}}_l$ **(kg/h)**	$\widetilde{T}_l$ **(°C)**
1	0%	4.39	168	0.8	62.5
2	61%	4.35	170		
3	90%	4.18	168		

5.1. Investigation of the heat flux

Figure 11 presents spatiotemporal maps of the tube temperature T_w measured by the IRT and the rate of heat flow per unit length removed by the internal mist flow along the blocked region Φ_{int}/L as a function of time of cooling for all the configurations. The value of Φ_{int}/L is calculated with the equation:

$$\frac{\Phi_{int}}{L} = \pi D_h \varphi_{int} \tag{10}$$

which uses the internal heat flux φ_{int} from Equation 3.

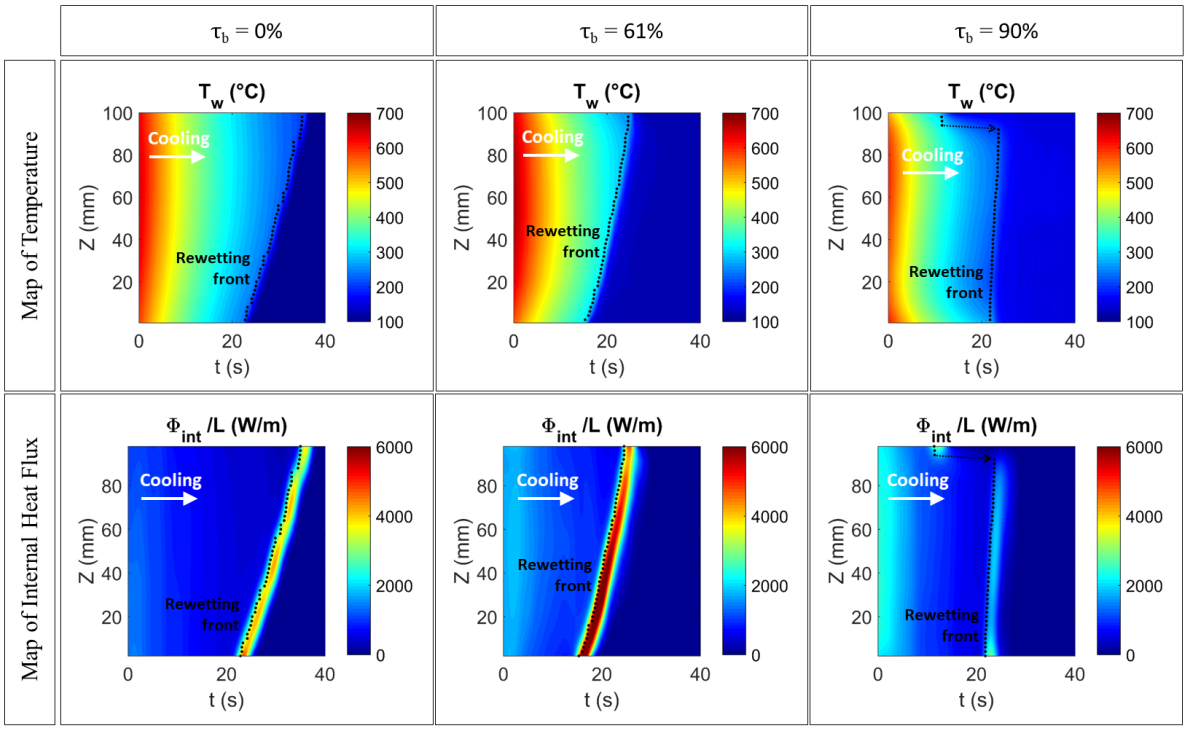

Figure 11: Spatiotemporal maps for the wall temperature T_w and the internal rate of heat flow per unit of length Φ_{int}/L for 0%, 61% and 90% blockage ratios.

For both cases, the internal heat flux decreases during the cooling phase until reaching a minimum followed by a peak where the heat transfer is maximum. This increase in the heat flux happens because of the rewetting phenomenon when droplets migrating towards the wall impinge on it directly and thus improves the heat dissipation by nucleate boiling. Beyond this peak during the cooling phase, the wall is completely wetted and, once again, Φ_{int}/L decreases with the rapid decrease in the wall temperature.

We used the same criterion of Xu [23] to define the rewetting front position, which consists of finding the minimum of the second derivative of the local temperature with respect to time ($\min(d^2T/dt^2)$). This is represented by dashed black lines in Figure 11, where we observe that it propagates from bottom to top inside the tube. For the case of the blockage ratio of 0%, the wall rewetting starts at 23 s and ends at 35 s. Meanwhile, it starts at 15 s and ends at 24 s with the 61% configuration. When we consider the blockage ratio of 90%, the rewetting at the bottom of the tube starts at 22 s and propagates to the top in less than 2 s. Therefore, keeping the same imposed steam and droplets mass flow rates in the sub-channel, the rewetting front propagates faster for higher blockage ratios. However, we

can see a discontinuity in the rewetting front at the end of the 90% blockage ratio tube, which may happen because of the steam flow separation in the expansion area of the tube that generates recirculation flows. Hence, in these zones, the droplets could be trapped and impinge the wall, improving the local heat transfer. Hishida et al have also observed this phenomenon in the case of a droplets-air flow in a backward facing step [24].

Afterwards, we collected points of T_w within ranges of 10 °C in the spatiotemporal map and their corresponding Φ_{int}/L (Fig. 11). Then, we calculated the respective arithmetic mean values $\widetilde{T}_w$ and $\widetilde{\Phi}_{int}/L$ using Equation 9 and plotted them as mean boiling curves for each geometry in Figure 12. For all the cases, a first process known as the Leidenfrost regime is observed where the heat flux decreases during the cooling phase with the wall temperature. Furthermore, during this regime, the heat flux increases with the blockage ratio because of the Venturi effect that accelerates the continuous steam phase in the reduction of the cross-sectional area and, consequently, the wall-to-steam convective heat transfer increases. The limit of this regime is reached when heat flux is minimum at the Leidenfrost temperature, which we found as 270 °C, 360 °C, and 260 °C for the blockage ratios of 0%, 61%, and 90% respectively. These different value for the Leidenfrost temperature are related to the droplets characteristics (both diameter and velocity) and the blockage geometry and will be discussed afterward in section 5.2.3. Beyond this minimum point during the cooling phase, the heat transfer is improved and the rewetting phenomenon takes place.

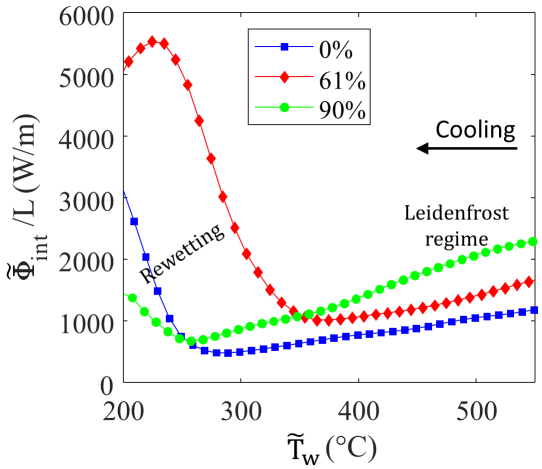

Figure 12: Mean rate of heat flow per unit length as a function of the mean wall temperature for each configuration.

As we mentioned in section 4.1.1, one of the hypotheses to estimate the internal heat dissipation by Eq. 3 is considering uniform temperature in the tube's azimuthal direction. This approach might not be true near the rewetting front location if it occurs non-uniformly, which creates high temperature gradients in the azimuthal direction. In the present work, we observed this non-uniform progress of the rewetting front only with the 61% configuration, as presented in Figure 13. The temperature in the azimuthal direction is almost constant after complete wall rewetting and during the Leidenfrost regime (up- and downstream of the rewetting front, respectively); however, this is not true at the rewetting front location. By consequence, because we did not consider any conductive heat transfer process in Eq. 3, the calculated internal heat dissipation might be overestimated near the minimum heat flux point in Figure 12.

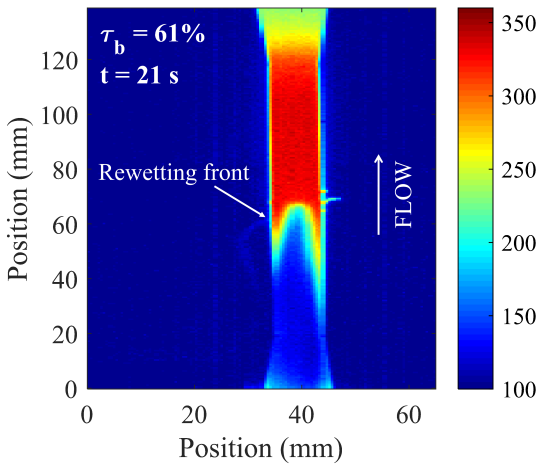

Figure 13: IRT image showing the advance of the rewetting front for the 61% blockage ratio tube (t = 21 s).

5.2. Dynamics of the dispersed phase

5.2.1. Properties of droplets upstream of the test section

Figure 14a shows the droplet diameter distributions upstream of the test section, being all the PDA measurements performed in the center of the tube cross-sectional area. For all the cases, we found a polydisperse distribution and mean droplet diameters of 110 μm, 88 μm and 100 μm for the respective blockage ratios of 0%, 61% and 90%. The results also show that the maximum detected droplet diameter is about 300 μm. Meanwhile, Figure 14b presents the droplets axial velocity as a function of the droplets diameter for each blockage ratio. We can notice that the droplet velocity does not change considerably with the droplet diameter upstream of the test section and its mean values are 16 m/s, 14.5 m/s and 12,5 m/s for a blockage of 0%, 61% and 90%, respectively. These results confirm that the droplets dynamic conditions upstream of the tube are quite similar for all the experiences and, therefore, the results downstream are mainly affected by the geometry.

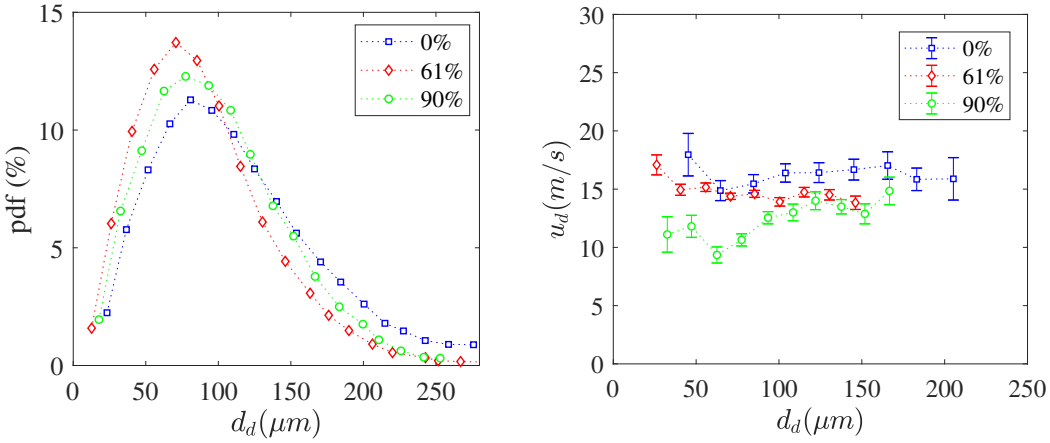

(a) (b)

Figure 14: Droplets dynamics upstream of the test section: (a) droplet diameter distribution of droplets (b) axial droplet velocity as a function of a droplet diameter.

5.2.2. Evolution of the droplets diameter distribution

Reminding that IRT and PDA techniques are synchronized during the cooling phase, we analyzed the PDA results downstream of the test section over a time interval corresponding to the mean axial wall temperature from $\overline{T}_w$=400 °C to $\overline{T}_w$=500 °C (i.e., in the Leidenfrost regime) using Equation 8. Hence, Figure 15 shows the droplets diameter distribution downstream for this tube temperature range. To better compare the evolution of the droplets dynamics, we overlapped in the figure the diameter distributions previously measured upstream.

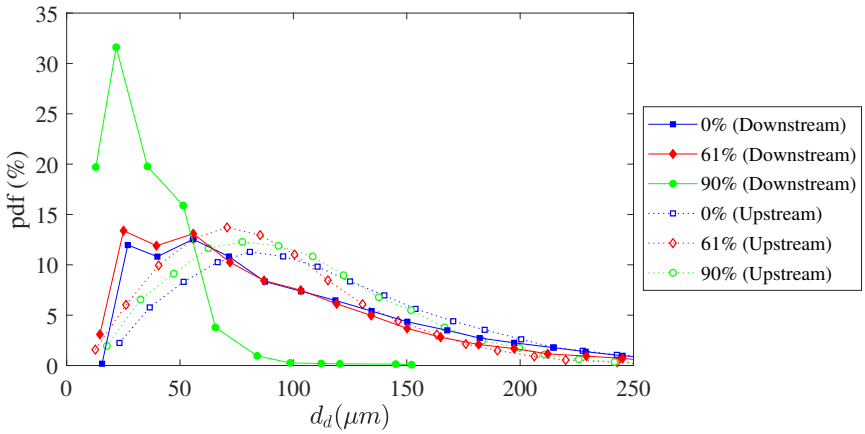

Figure 15: Droplet diameter distribution downstream for a wall temperature interval of 400 °C $\leq \overline{T}_w \leq$ 500 °C.

For the blockage ratios of 0% and 61%, the distributions downstream exhibit a shift of approximately 20% towards smaller droplets diameters compared to the case upstream because of the droplet evaporation phenomenon in the test section, giving the respective mean droplet diameters of 90 μm and 70 μm. With a 90% blockage ratio, we can observe a larger shift toward smaller droplets downstream, with a mean value of 25 μm, because of droplets breakup in the test section. Indeed, because of the acceleration of the steam flow in the blocked region, a substantial difference between the steam and the droplets velocity (u_s-u_d) could lead to hydrodynamic instabilities and thus to the droplets breakup. We can confirm this statement by estimating the Weber number We_d at the beginning of the blockage zone with the following expression:

$$We_{d,j} = \frac{\rho_s \left(u_s - u_{d,j}\right)^2 d_{d,j}}{\sigma_d} \tag{11}$$

with ρ_s the steam density, $u_{d,j}$ the droplet velocity for the diameter class j obtained by PDA measurements upstream (Figure 14b), and σ_d the liquid surface tension. The steam velocity at the blockage zone u_s is estimated by isothermal mass conservation, i.e. considering the steam temperature does not change (neither its density) when passing through the converging part of the test section, which gives the following expression:

$$u_s = \frac{\dot{m}_s}{\rho_s S_b} \tag{12}$$

According to several studies in the literature, breakup takes place for $We_{d,crit} \geq 12$ [25–27]. Some authors suggest

a dependence of this critical value on the droplet Reynolds number Re_d, as Brauer's correlation [27] given by:

$$We_{d,crit} = 55\left(\frac{24}{Re_d} + \frac{20.2}{Re_d^{0.615}} - \frac{16}{Re_d^{2/3}}\right) \tag{13}$$

Figure 16 shows the Weber number estimated using Equation 11 as a function of the droplets Reynolds number, as well as the critical Weber numbers mentioned before. The droplets Reynolds number Re_d, j in the blockage zone is calculated for each diameter class $d_{d,j}$ according to the PDA measurements upstream of Part II and is defined as:

$$Re_{d,j} = \frac{\rho_s\,(u_s - u_{d,j})\,d_{d,j}}{\mu_s} \tag{14}$$

The results show that there is no droplets breakup with the blockage ratios of 0% and 61%. However, droplets breakup can take place for a blockage of 90% for diameters larger than 70 μm, resulting in the significant shift towards the smaller droplets observed in Figure 15.

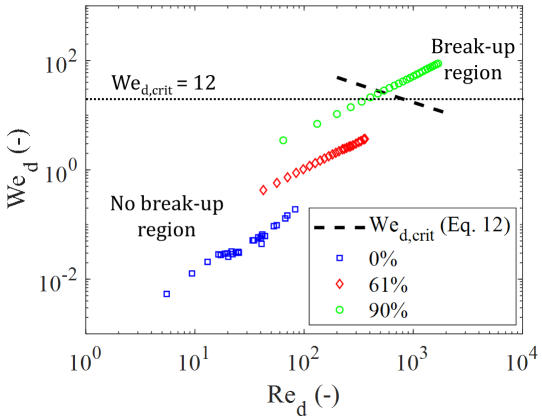

Figure 16: Weber number as a function of Reynolds number

One could think that droplets breakup would also occur due to splashing after impacting onto the wall. In the literature, we find that droplets splashing only occurs if the Mundo number ($K_M = \sqrt{We}Re^{0.25}$) of the droplet impact is higher than 380 when the wall temperature is above the Leidenfrost point [28, 29]. For the present case, the worst-case scenario where K_M is the highest would occur with the largest droplet ($d_d = 300$ μm) passing through the converging region of Part II, which has an angle of 6 ° (Figure 6). Considering the droplet axial velocity of 20 m/s, which is nearly the highest value observed in Figure 14b, the normal velocity for the impact would be of 2.1 m/s, resulting in $K_M \approx 24$, which is much below the limit to occur splashing. Therefore, all the droplets impacting onto the heated wall bounces away with no breakup.

5.2.3. Evolution of the droplets velocity

Figure 17 presents the droplets axial velocity as a function of the droplets diameter downstream of the test section. Once again, we overlapped in the figure the results found upstream for a better analysis of the droplet dynamics evolution. For all cases, droplets velocity downstream is higher than upstream and, furthermore, it is dependent on the droplets diameter: smaller droplets have higher velocities than larger ones. In addition, the droplets velocity

increases with the blockage ratio and the mean values are 23 m/s, 38 m/s, and 90 m/s for the blockages of 0%, 61% and 90%, respectively.

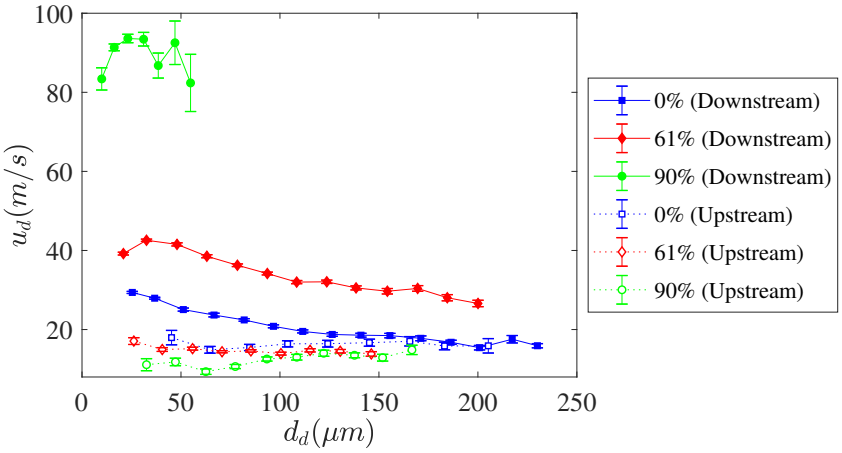

Figure 17: Droplets axial velocity as a function of droplets diameter for a wall temperature interval of 400 °C $\leq \overline{T}_w \leq$500 °C.

This large difference occurs because of the increased steam velocity in the blockage zone due to the Venturi effect, which results in stronger drag forces on the droplets and, consequently, their acceleration. For comparison, by using Equation 12 we find that the steam velocities for the 61% and 90% blockage ratios are, respectively, 57.7 m/s and 216 m/s. Meanwhile, its velocity upstream of Part II (and in the 0% blockage ratio tube) is 22.7 m/s. However, the droplets velocity is not as high as the steam velocity because of their high inertia. This is confirmed when calculating the droplets Stokes number St_d, which is the ratio of the characteristic times of the droplet and the flow and is defined by:

$$St_{d,j} = \left(\frac{\rho_d d_{d,j}^2}{18\mu_s}\right)\frac{(u_s - u_{d,j})}{L_b} \tag{15}$$

where ρ_d is the liquid density and μ_s is the steam dynamic viscosity. The steam velocity u_s is calculated with Equation 12, while the droplets velocity $u_{d,j}$ is the mean value of the measured up- and downstream of Part II. The droplets diameters $d_{d,j}$ are those measured downstream of Part II. Figure 18 shows the calculated Stokes number as a function of the droplets diameter for each configuration in the blockage zone. In the literature, we find that droplets with $\mathrm{St}_d \ll 1$ have low inertia and follow the steam flow closely, while droplets with $\mathrm{St}_d \gg 1$ are inertial and are much less affected by the Venturi effect [30]. As most of the droplets are inertial, they are accelerated by the steam in the blockage zone but without reaching the terminal velocity. This analysis explains the values observed with the PDA system downstream of Part II, as well as the decreasing droplets velocity with the increasing droplets diameter.

As seen before in Fig. 12, the Leidenfrost temperature is different for each geometry (270 °C, 360 °C, and 260 °C for a blockage ratio of 0%, 61%, and 90% respectively) and this can be explained by the droplets characteristics observed in Fig. 15 and 17. The higher the droplets velocity, the higher their kinetic energy in eventual droplet-wall interactions that might take place because of the turbulent flow. Consequently, wall rewetting may occur with higher wall temperatures, as observed as well by Dunand et al [31]. This might explain the increase in the Leidenfrost

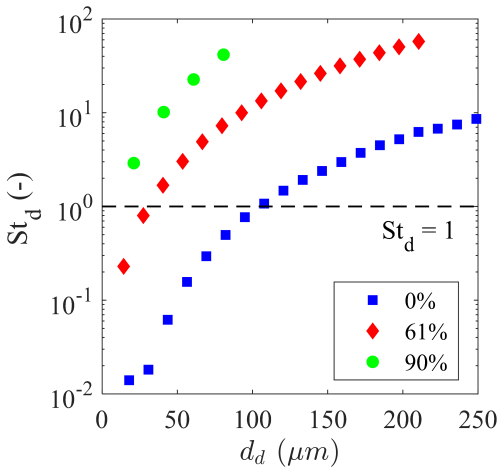

Figure 18: Stokes number as a function of the droplet diameter for each blockage ratio.

temperature found for the 61% blockage ratio compared with the 0%.

Nevertheless, the Leidenfrost temperature decreases again with 90% blockage ratio, even though the droplets velocity is substantially higher. This is because of the droplets breakup that happens only with the 90% blockage ratio case, as already discussed in Fig. 15 and 16. Smaller droplets have smaller kinetic energy and, therefore, wall rewetting occurs with lower wall temperatures. Meholic et al observed similar behavior in their mechanistic model, showing that smaller droplets have their trajectory changed near the heated wall and no impact occurs with higher wall temperatures [11].

5.2.4. Droplets mean temperature

As we mentioned in section 4.3, we performed the 3cLIF measurements before starting the cooling phase (moment 3 in Figure 7) up- and downstream of the test section. Equation 9 was used to calculate the droplets mean temperature $\widetilde{T}_d$, being about 400 the number of collected droplets for each measurement, and we present the results in Figure 19.

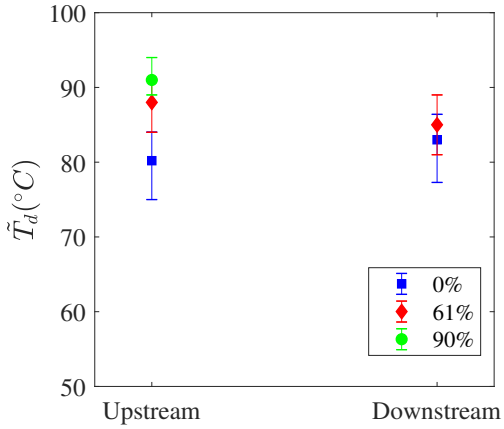

Figure 19: Mean droplets temperature up- and downstream of the test section using LIF technique.

Although the droplets are injected at about 62 °C (Table 4), they are heated by the steam flow until arriving at the optical access upstream of the test section, where they reach the temperature of approximately 85 °C, according

to the 3cLIF measurements. The mean droplets temperatures are approximately the same up- and downstream of the test section and close to saturation. Therefore, we can consider the droplets are in nearly thermal equilibrium and the heat transfer between steam and droplets in the test section is completely targeted to the evaporation of droplets, which was also confirmed by PDA results in Figure 15.

For a blockage ratio of 90%, no droplets have been detected by the LIF detection chain. Indeed, due to the high droplet velocity (over 80 m/s), their transit time in the laser excitation volume is too short to be detected by the LIF acquisition board, which has certainly too low frequency of sampling for this velocity.

6. Conclusions

This work presented an experimental study of the cooling phase in a vertical pipe with an internal steam-droplets flow, aiming to represent at sub-channel scale the conditions found during a LOCA in a nuclear reactor. The blockage ratio effect was analyzed on both the heat dissipation and the droplets characteristics. Three main techniques allowed a broad characterization of the process: IRT for the tube temperature decrease, PDA for the droplets diameter and velocity, and 3cLIF for the droplets mean temperature. The main findings are listed below:

- The cooling of the tube begins in the Leidenfrost regime, where the rate of heat dissipated by the internal flow decreases with the decrease in the wall temperature. With the wall rewetting, a sharp increase in the heat dissipation is observed.
- In general, wall rewetting takes place from bottom to top in the test section. Nevertheless, for the case of 90% blockage ratio, rewetting also occurred immediately after the blockage in the tube, possibly because of the steam flow separation in the expansion that generates recirculation flows.
- Because of the Venturi effect and because the imposed flow rate at the inlet of the test section is the same regardless of the configuration (contrary to the expected in case of a LOCA), the heat dissipation is higher with the increase in the blockage ratio in the Leidenfrost regime.
- Evaporation causes the decrease in the droplets diameter downstream of the test section, as observed with the blockage ratios of 0% and 61%. This reduction is more significant with the 90% blockage ratio because of droplets breakup due to hydrodynamic instabilities.
- Because of drag forces, the droplets velocity is always higher downstream of the test section than upstream, being this increase more significant with the increase in the blockage ratio. Moreover, the larger the droplets diameter, the lower the droplets velocity downstream of the test section.
- Eventually, no significant change in the droplets mean temperature was observed, which indicates nearly thermal equilibrium state of the liquid phase in the two-phase flow.

7. Further work

It is important to outline that these experimental data and results, although valuable for future validation of mechanistic models, must not be extrapolated to a situation of LOCA in a nuclear reactor scale. This is because

the present work is at sub-channel scale and by-pass effects are not simulated, which might change substantially the blockage ratio effect. Complementary work is needed to take into account phenomena at fuel bundle scale.

8. Funding

This work is completed within the framework of RSNR Project PERFROI from a French State aid managed by the French National Research Agency under the program of Investments for the Future carrying the reference n° ANR-11-RSNR-0017.

References

[1] United States Nuclear Regulatory Commission, 10 C.F.R. §50.46 (2017).

[2] G. Repetto, C. Dominguez, B. Durville, S. Carnemolla, D. Campello, C. Tardif, M. Gradeck, The R&D PERFROI project on thermal mechanical and thermal hydraulics behaviors of a fuel rod assembly during a loss of coolant accident, International Topical Meeting on Nuclear Reactor Thermal Hydraulics 2015, NURETH 2015 1 (2015) 1–14.

[3] K. Kim, B. J. Kim, H. S. Choi, S. K. Moon, C. H. Song, Effect of a blockage length on the coolability during reflood in a 2 x 2 rod bundle with a 90% partially blocked region, Nuclear Engineering and Design 312 (2017) 248–255. doi:10.1016/j.nucengdes.2016.08.031.

[4] P. Ruyer, N. Seiler, B. Biton, F. Lelong, F. Secondi, D. Baalbaki, M. Gradeck, Two-phase flow across a partially damaged core during the reflood phase of a loca, Nuclear Engineering and Design 264 (2013) 187 – 194, sI:NURETH-14. doi:https://doi.org/10.1016/j.nucengdes.2013.02.026.
URL http://www.sciencedirect.com/science/article/pii/S002954931300085X

[5] R. Lee, J. Reyes, K. Almenas, Size and number density change of droplet populations above a quench front during reflood, International Journal of Heat and Mass Transfer 27 (4) (1984) 573 – 585. doi:https://doi.org/10.1016/0017-9310(84)90030-9.
URL http://www.sciencedirect.com/science/article/pii/0017931084900309

[6] C. Grandjean, Coolability of blocked regions in a rod bundle after ballooning under loca conditions: Main findings from a review of past experimental programmes, Nuclear Engineering and Design 237 (15) (2007) 1872 – 1886, nURETH-11. doi:https://doi.org/10.1016/j.nucengdes.2007.02.022.
URL http://www.sciencedirect.com/science/article/pii/S0029549307002038

[7] H. K. Cho, K. Y. Choi, S. Cho, C.-H. Song, Experimental observation of the droplet size change across a wet grid spacer in a 6x6 rod bundle, Nuclear Engineering and Design 241 (12) (2011) 4649 – 4656, the18th International Conference on Nuclear Engineering (ICONE-18). doi:https://doi.org/10.1016/j.nucengdes.2011.03.042.
URL http://www.sciencedirect.com/science/article/pii/S0029549311002548

[8] Z. Hózer, I. Nagy, M. Kunstár, P. Szabó, N. Vér, R. Farkas, I. Trosztel, A. Vimi, Experimental investigation of the coolability of blocked hexagonal bundles, Nuclear Engineering and Design 317 (2017) 51 – 58. doi:https://doi.org/10.1016/j.nucengdes.2017.03.030.
URL http://www.sciencedirect.com/science/article/pii/S0029549317301425

[9] Y. Jin, F. R. Beck, B. R. Lowery, D. J. Miller, F. B. Cheung, S. M. Bajorek, K. Tien, C. L. Hoxie, Experimental study of droplet sizes across a spacer grid location under various reflood conditions, Experimental Thermal and Fluid Science 94 (February 2017) (2018) 246–257. doi:10.1016/j.expthermflusci.2018.02.017.

[10] Y. Guo, K. Mishima, A non-equilibrium mechanistic heat transfer model for post-dryout dispersed flow regime, Experimental Thermal and Fluid Science 26 (6-7) (2002) 861–869. doi:10.1016/S0894-1777(02)00195-4.

[11] M. J. Meholic, D. L. Aumiller, F. B. Cheung, A comprehensive, mechanistic heat transfer modeling package for dispersed flow film boiling - part 2 - implementation and assessment, Nuclear Engineering and Design 291 (2015) 302–311. doi:10.1016/j.nucengdes.2015.07.014.

[12] T. Glantz, T. Taurines, O. D. Luze, S. Belon, G. Guillard, F. Jacq, Draccar: A multi-physics code for computational analysis of multi-rod ballooning, coolability and fuel relocation during loca transients part one: General modeling description, Nuclear Engineering and Design 339 (2018) 269 – 285. doi:https://doi.org/10.1016/j.nucengdes.2018.06.022.
URL http://www.sciencedirect.com/science/article/pii/S0029549318307003

[13] C. Grandjean, A state-of-the-art review of past programs devoted to fuel behaviour under loca conditions - part1: Clad swelling and rupture assembly flow blockage, Technical report, IRSN/DPAM/SEMCA (2005).

[14] Y. Jin, F.-B. Cheung, S. M. Bajorek, K. Tien, C. L. Hoxie, Investigation of the thermal-hydraulic non-equilibrium in a 7x7 rod bundle during reflood, International Journal of Heat and Mass Transfer 127 (2018) 266 – 279. doi:https://doi.org/10.1016/j.ijheatmasstransfer.2018.08.011.
URL http://www.sciencedirect.com/science/article/pii/S0017931018325808

[15] Y. A. Çengel, A. J. Ghajar, Heat and Mass Transfer: Fundamentals and Applications, McGraw-Hill Education, 2015.

[16] H. Albrecht, N. Damaschke, M. Borys, C. Tropea, Laser Doppler and Phase Doppler Measurement Techniques, Experimental Fluid Mechanics, Springer-Verlag Berlin Heidelberg, 2003.
URL https://www.springer.com/la/book/9783540678380

[17] A. Labergue, J.-D. Pena-Carillo, M. Gradeck, F. Lemoine, Combined three-color LIF-PDA measurements and infrared thermography applied to the study of the spray impingement on a heated surface above the leidenfrost regime, International Journal of Heat and Mass Transfer 104 (2017) 1008 – 1021. doi:https://doi.org/10.1016/j.ijheatmasstransfer.2016.07.029.
URL http://www.sciencedirect.com/science/article/pii/S0017931016319561

[18] A. Labergue, A. Delconte, F. Lemoine, Study of the thermal mixing between two non-isothermal sprays using combined three-color LIF thermometry and phase doppler analyzer, Experiments in Fluids 54 (6) (2013) 1527. doi:10.1007/s00348-013-1527-1.
URL https://doi.org/10.1007/s00348-013-1527-1

[19] G. Castanet, P. Lavieille, M. Lebouché, F. Lemoine, Measurement of the temperature distribution within monodisperse combusting droplets in linear streams using two-color laser-induced fluorescence, Experiments in Fluids 35 (6) (2003) 563–571. doi:10.1007/s00348-003-0702-1.
URL https://doi.org/10.1007/s00348-003-0702-1

[20] A. Labergue, V. Deprédurand, A. Delconte, G. Castanet, F. Lemoine, New insight into two-color LIF thermometry applied to temperature measurements of droplets, Experiments in Fluids 49 (2) (2010) 547–556. doi:10.1007/s00348-010-0828-x.
URL https://doi.org/10.1007/s00348-010-0828-x

[21] A. Labergue, A. Delconte, G. Castanet, F. Lemoine, Study of the droplet size effect coupled with the laser light scattering in sprays for two-color LIF thermometry measurements, Experiments in Fluids 52 (5) (2012) 1121–1132. doi:10.1007/s00348-011-1242-8.
URL https://doi.org/10.1007/s00348-011-1242-8

[22] V. Deprédurand, P. Miron, A. Labergue, M. Wolff, G. Castanet, F. Lemoine, A temperature-sensitive tracer suitable for two-colour laser-induced fluorescence thermometry applied to evaporating fuel droplets, Measurement Science and Technology 19 (10) (2008) 105403.
URL http://stacks.iop.org/0957-0233/19/i=10/a=105403

[23] J. Xu, Flow boiling heat transfer in the quenching of a hot surface under reduced gravity conditions, Ph.D. thesis, University of Toronto (1998).

[24] K. Hishida, T. Nagayasu, M. Maeda, Augmentation of convective heat transfer by an effective utilization of droplet inertia, International Journal of Heat and Mass Transfer 38 (10) (1995) 1773–1785. doi:10.1016/0017-9310(94)00308-I.

[25] M. Pilch, C. Erdman, Use of breakup time data and velocity history data to predict the maximum size of stable fragments for acceleration-induced breakup of a liquid drop, International Journal of Multiphase Flow 13 (6) (1987) 741 – 757. doi:https://doi.org/10.1016/0301-9322(87)90063-2.
URL http://www.sciencedirect.com/science/article/pii/0301932287900632

[26] T. Kékesi, G. Amberg, L. Prahl Wittberg, Drop deformation and breakup, International Journal of Multiphase Flow 66 (2014) 1 – 10. doi:https://doi.org/10.1016/j.ijmultiphaseflow.2014.06.006.
URL http://www.sciencedirect.com/science/article/pii/S0301932214001141

[27] N. I. Kolev, Multiphase Flow Dynamics, 4th Edition, Vol. 2, Springer, Berlin, 2011.

[28] M. Gradeck, N. Seiler, P. Ruyer, D. Maillet, Heat transfer for leidenfrost drops bouncing onto a hot surface, Experimental Thermal and Fluid Science 47 (2013) 14 – 25. doi:https://doi.org/10.1016/j.expthermflusci.2012.10.023.

[29] G. Castanet, T. Liénart, F. Lemoine, Dynamics and temperature of droplets impacting onto a heated wall, International Journal of Heat and Mass Transfer 52 (3) (2009) 670 – 679. doi:https://doi.org/10.1016/j.ijheatmasstransfer.2008.07.024.
URL http://www.sciencedirect.com/science/article/pii/S0017931008004328

[30] C. Crowe, J. Schwarzkopf, M. Sommerfeld, Y. Tsuji, Multiphase Flows with Droplets and Particles, Taylor & Francis, 1997.

[31] P. Dunand, G. Castanet, M. Gradeck, D. Maillet, F. Lemoine, Energy balance of droplets impinging onto a wall heated above the leidenfrost temperature, International Journal of Heat and Fluid Flow 44 (2013) 170 – 180. doi:https://doi.org/10.1016/j.ijheatfluidflow.2013.05.021.
URL http://www.sciencedirect.com/science/article/pii/S0142727X13001306